Journal of Power Sources 196 (2011) 246–254

Contents lists available at ScienceDirect

Journal of Power Sources

journal homepage: www.elsevier.com/locate/jpowsour

Effective thermal conductivity and thermal contact resistance of gas diffusion layers in proton exchange membrane fuel cells. Part 1: Effect of compressive load

E. Sadeghi [a,b,*], N. Djilali [a], M. Bahrami [b]

[a] Dept. Mechanical Eng., and Institute for Integrated Energy Systems, University of Victoria, P.O. Box 3055, Victoria, BC, Canada V8W 3P6
[b] Mechatronic Systems Engineering, School of Engineering Science, Simon Fraser University, Surrey, BC, Canada V3T 0A3

ARTICLE INFO

Article history:
Received 7 May 2010
Received in revised form 11 June 2010
Accepted 11 June 2010
Available online 20 June 2010

Keywords:
TCR
Interface
Effective thermal conductivity
Conduction
Compression

ABSTRACT

Heat transfer through the gas diffusion layer (GDL) is a key process in the design and operation of a PEM fuel cell. The analysis of this process requires determination of the effective thermal conductivity as well as the thermal contact resistance associated with the interface between the GDL and adjacent surfaces/layers.

In the present study, a custom-made test bed that allows the separation of effective thermal conductivity and thermal contact resistance in GDLs under vacuum and ambient conditions is described. Measurements under varying compressive loads are performed using Toray carbon paper samples with a porosity of 78% for a range of thicknesses. The measurements are complemented by compact analytical models that achieve good agreement with experimental data. A key finding is that thermal contact resistance is the dominant component of the total thermal resistance; neglecting this phenomenon may result in significant errors in evaluating heat transfer rates and temperature distributions.

1. Introduction

The electrochemical reaction and associated irreversibilities in a proton exchange membrane (PEM) fuel cell generate a substantial amount of heat that results in temperature gradients in various components of a cell [1–4]. The product heat has to be extracted from the cell to maintain optimal working conditions; indeed the implementation of efficient and reliable cooling strategies for PEM fuel cells is crucial to ensure high efficiency, reliability and durability.

Accurate knowledge of the temperature distribution and associated heat transfer mechanisms is required to determine various transport phenomena such as water and species transport, reaction kinetics, and rate of phase change. For instance, saturation pressure, which determines phase equilibrium between liquid water and gas phases in both the gas flow channels and porous media of a fuel cell, varies non-linearly with temperature. A thermal analysis is also required to assess thermal-related phenomena in the gas diffusion layer (GDL) and the catalyst layer that can induce hygro-thermal stress and material degradation, and compromise performance and lifetime [5,6]. Any successful fuel cell thermal analysis requires two key transport coefficients: (i) the effective thermal conductivity of the gas diffusion layer (GDL) as a function of the micro-structural geometry of the GDL and the operating conditions, e.g. compressive load and temperature and (ii) the thermal contact resistance (*TCR*). The latter is an interfacial phenomenon arising due to imperfect contact at the interface between the GDL and the solid surface of the bipolar plates as well as at the catalyst layer–GDL interface. Considering the small thickness of the components that make up the membrane–electrode-assembly, and the very distinct surface morphology of the membrane, catalyst layer and GDL, interfacial transport phenomena are expected to have a significant impact in general, and *TCR* in particular can give rise to a significant resistance which will limit heat transfer rates through the GDL.

Generally, all surfaces have roughness and out-of-flatness at the microscale level, and the actual contact area is thus only a fraction of the nominal contact area [7]. In GDLs with high porosity, this scenario is even worse, with actual contact area expected to be less than 1% of the nominal cross-sectional area. In addition, the complexity and anisotropy of the GDL micro-structure make it intricate to define accurate values for *TCR* and the effective thermal conductivity.

Large differences in thermal conductivity of solid and fluid phases as well as high porosity of GDL micro-structure make it necessary to define an effective thermal conductivity, a transport parameter that plays an important role in fuel cell performance analysis [8] and that is required in computational models [9]. A few studies in the literature have focused on the analytical model-

* Corresponding author at: Dept. Mechanical Eng., and Institute for Integrated Energy Systems, University of Victoria, P.O. Box 3055, Victoria, BC, Canada V8W 3P6. Tel.: +1 7787828587; fax: +1 2507216051.
E-mail address: ehsans@uvic.ca (E. Sadeghi).

0378-7753/$ – see front matter © 2010 Elsevier B.V. All rights reserved.
doi:10.1016/j.jpowsour.2010.06.039

Nomenclature

A	cross-sectional area (m^2)
A_0	nominal contact area (m^2)
a	major semi-axis of contact area (m)
b	minor semi-axis of contact area (m)
D_{peak}	peak density of surface (m^{-1})
d	fiber mean diameter (m)
E	Young's modulus (Pa)
E^*	effective Young's modulus (Pa)
F	force (N)
h	separation of contacting surfaces (m)
k	thermal conductivity ($W\,m^{-1}\,K^{-1}$)
k_{eff}	effective thermal conductivity ($W\,m^{-1}\,K^{-1}$)
N	number of microcontacts
P_0	reference contact pressure (Pa)
P_{atm}	atmospheric pressure (Pa)
P_c	contact pressure (Pa)
P_c^*	dimensionless contact pressure
P_g	gas pressure (Pa)
Q	heat transfer rate (W)
R_e	effective radius of contacting bodies (m)
R_{GDL}	GDL thermal resistance ($K\,W^{-1}$)
R_p	asperity radius (m)
R_{sp}	thermal spreading resistance ($K\,W^{-1}$)
R_{tot}	total thermal resistance ($K\,W^{-1}$)
r	fiber mean radius (m)
T	temperature (K)
TCR	thermal contact resistance ($K\,W^{-1}$)
t	sample thickness (m)
t_0	nominal sample thickness (m)
z	height (m)

Greek symbols

α	aspect ratio of the contact area (ba^{-1})
ε	strain ($\Delta t \cdot t_0^{-1}$)
σ	root mean square of the surface roughness
ν	Poisson's ratio
λ	onset of elastic deformation (m)
δ	deviation in parameters
δ_e	elastic deformation (m)
δ_s	thickness reduction caused by fiber slippage (m)
δ_{tot}	total thickness reduction (m)
$\kappa(\cdot)$	elliptic integral of the first kind
$\psi(\cdot)$	constriction parameter
$\phi(\cdot)$	normal distribution

Subscripts

1	sample 1
2	sample 2
c	carbon fiber
fl	fluxmeter
low	lower contact surface
up	upper contact surface
uc	unit cell

ing of GDL thermal conductivity. Ramousse et al. [8] investigated the effective thermal conductivity of non-woven carbon felt GDLs and estimated the conductivity bounds using a model connecting the two phases (solid and gas) in series or parallel. They used Danes and Bardon correlation [10] to estimate the effective thermal conductivity of the solid phase. The model as well as the experimental measurements yielded conductivity values that are lower than most values reported in the literature. Using the unit cell concept, the present authors recently presented a compact analytical model to determine the effective thermal conductivity of GDLs [11]. A micro-structure of uniformly sized, equally spaced cylindrical fibers immersed in stagnant air was assumed, and the Hertzian theory [7] was used to calculate the contact area between the touching fibers, considering a range of fiber angles. The analysis was performed by constructing a thermal resistance network that takes into account the thermal paths through solid fibers (constriction and spreading resistance) and air (rarefaction effects).

The complexity of the GDL micro-structure and associated challenges in obtaining analytic solutions have lead most researchers toward numerical [12,13] and experimental methods [14–16]. Becker et al. [12] used 3D tomography to reconstruct a GDL and a numerically efficient pore morphology method to determine phase distributions and to deduce permeability, diffusivity and thermal conductivity as a function of the saturation under different compressive loads. Wang et al. [13] developed a numerical method based on the Lattice Boltzmann technique to predict the effective thermal conductivity of randomly fibrous media. Assuming a two-dimensional stochastic and random micro-structure, a generation-growth method was employed to reconstruct the porous medium based on diameter, length, core position, and alignment of each fiber.

Khandelwal and Mench [14] measured the through-plane thermal conductivity of GDLs by examining two different types of commercial GDLs with a variety of thicknesses and porosities. They studied the effect of temperature and polytetrafluoroethylene (PTFE) content on the effective thermal conductivity, and obtained values in close agreement with the manufacturer data. The effect of pressure on effective thermal conductivity was investigates by Nitta et al. [15] using a guarded-hot-plate apparatus and SGL SIGRACET® 10 BA GDL samples. The GDL thickness under compressive loads was monitored using a dial indicator. The thermal conductivity was found to be independent of compression. Using a similar apparatus, Burheim et al. [16] measured the effective thermal conductivity of uncoated SolviCore gas diffusion layers under various compaction pressures. They presented a methodology to find thermal conductivity and thermal contact resistance (*TCR*) and results showing that the effective thermal conductivity increases with compressive load while *TCR* decreases.

The available studies on thermal contact resistance of GDLs in the literature are limited to experimental measurements and there is a lack of analytical investigations in this field. However, several pertinent analytical and experimental approaches have been reported on electrical contact resistance [17–20]. These studies have employed fractal based models [17] or the Hertzian elastic theory [18–20] to find the contact area between the asperities of GDL and bipolar plate/catalyst layer surfaces and have the potential of being extended to thermal analysis.

A review of the literature indicates that in the majority of previous studies related to heat transfer in GDL, the *TCR* was 'bundled up' with the effective thermal conductivity and characterized using an aggregate value. One fundamental issue with combining the two is that *TCR* is an *interfacial phenomenon* that is a function of mechanical load and surface characteristics of both interfacing surfaces, whereas thermal conductivity is a transport coefficient characterizing the *bulk* medium. Thermal conductivity and *TCR* should therefore be distinguished. Furthermore, the effect of compressive load on thermal conductivity and *TCR* has not been thoroughly investigated.

The experimental technique developed in this study allows the deconvolution of *TCR* and thermal conductivity and was used to perform a comprehensive experimental study:

- to determine through-plane thermal conductivity of GDLs as a function of porosity, compressive load, and temperature; and
- to measure the thermal contact resistance at the interface of GDL and a solid surface as a function of mechanical load and porosity.

A custom-made test bed was designed and built that enables the measurements of thermal conductivity and *TCR* of porous media under vacuum and ambient pressure conditions. The test bed was equipped with a loading mechanism that allows the application of various compressive loads on the samples. Toray carbon papers with the porosity of 78% and different thicknesses are used in the experiments. The effect of ambient and compression is investigated, and includes measurement of the GDL thickness variation using a tensile-compression apparatus. The effective thermal conductivity and *TCR* are deduced from the total thermal resistance measurements by performing a series of experiments with GDL samples of various thicknesses and similar micro-structures. The effect of operating temperature (35–70 °C) on both thermal conductivity and *TCR* is also investigated. Furthermore, analytical models are developed to evaluate through-plane thermal conductivity of GDLs as well as the thermal contact resistance at the interface of GDL and a solid surface as a function of the compressive load. These models are compared against the experimental data obtained in this study.

2. Experimental study

2.1. Thermal test

The experimental apparatus and a schematic of the test column in the test chamber are shown in Fig. 1. The test chamber consists of a stainless steel base plate and a bell jar enclosing the test column. The test column consists of, from top to bottom: the loading mechanism, the steel ball, the heater block, the upper heat fluxmeter, the sample, the lower fluxmeter, the heat sink (cold plate), the load cell, and the polymethyl methacrylate (PMMA) layer. The heater block consists of circular flat copper in which cylindrical pencil-type electrical heaters are installed. The power to the heaters can be adjusted manually. In the present study, a 30 W Omega heater is used. It should be noted that the determination of the thermal conductivity and thermal contact resistance are independent of the heat flux setting through the sample, and that for the purpose of such measurements this heat flux need not be related to the heat generated in an operating fuel cell. The setting of the heater was selected to be sufficiently high to provide good temperature resolution, while ensuring that the temperature in the samples remained in a range representative of fuel cell operation.

The designed cold plate consists of a hollow copper cylinder, 1.9 cm high and 15 cm diameter. Cooling is accomplished using a closed loop water–glycol bath in which the coolant temperature can be set. The cold plate is connected to the chiller unit which adjusts the cold water temperature. A 1000 lb load cell is used to measure the applied load to the joint. The load is applied over a load button placed at the center of the load cell.

The fluxmeters were made of a standard electrolyte iron material. To measure temperatures six T-type thermocouples were attached to each fluxmeter at specific locations shown in Fig. 1. The thermal conductivity of the iron fluxmeter was known and used to measure the heat flow rate transferred through the contact region.

2.1.1. Sample preparation

Toray carbon papers TGP-H-120 and TGP-H-060 with the porosity of 78% were used. These samples have 5% wet proofing and their thicknesses are 0.37 mm and 0.19 mm, respectively. The samples were cut in circles with 25 mm diameter and sandwiched between

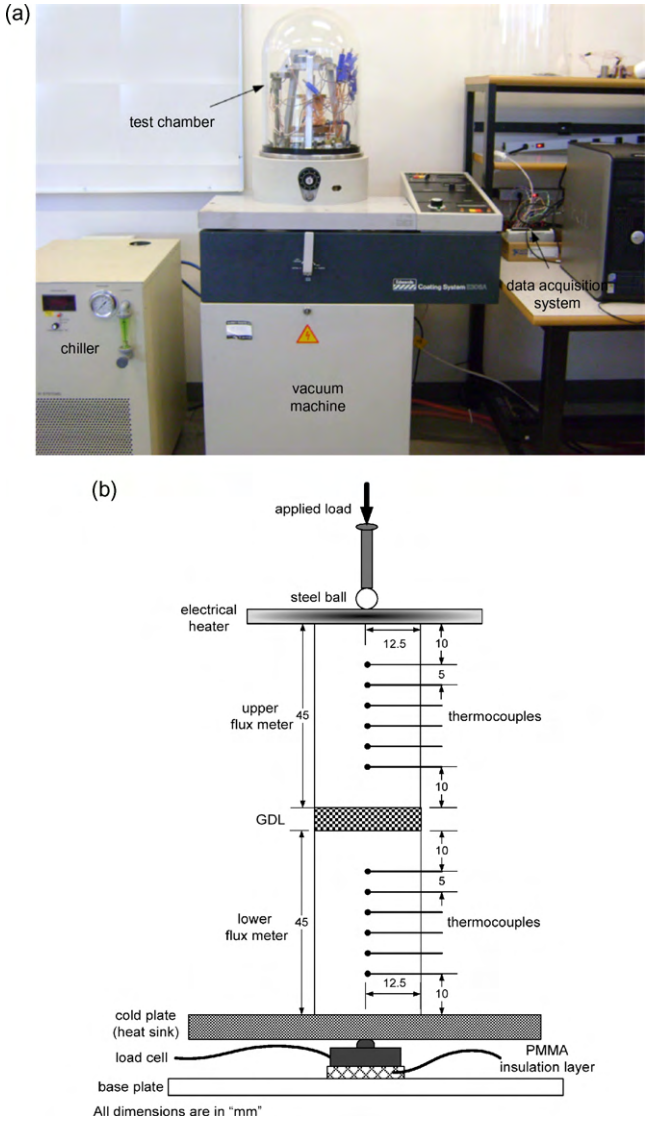

Fig. 1. (a) Experimental apparatus used for thermal conductivity and *TCR* test bed and (b) schematic view of the test column.

the fluxmeters. Fig. 2 shows scanning electron microscopy (SEM) images of the carbon papers before loading.

2.1.2. Test procedure

Experiments were conducted under vacuum and ambient conditions. A vacuum level of 10^{-5} mbar was achieved under the test chamber using the vacuum machine. To minimize heat transfer to the surrounding, the test column including the fluxmeters and samples was insulated using glass wool insulation layers. Temperatures and pressure were recorded at various compressive loads when steady-state conditions were achieved; to reach thermal equilibrium, all the experiment's parameters were kept constant and carefully monitored for approximately 4–5 h for each data point. The effects of compression were investigated over the range 0.2–1.5 MPa, i.e. up to values that correspond to the highest pressures transmitted in practice to the GDL from the current collecting plates [21].

The temperature gradient between the hot and cold plates results in essentially one-dimensional heat conduction from the top to the bottom of the test column. The temperature distribution is therefore stabilizing, and since the Grashof number is of the order of 10^{-6}, which is significantly lower than the critical value of 2500

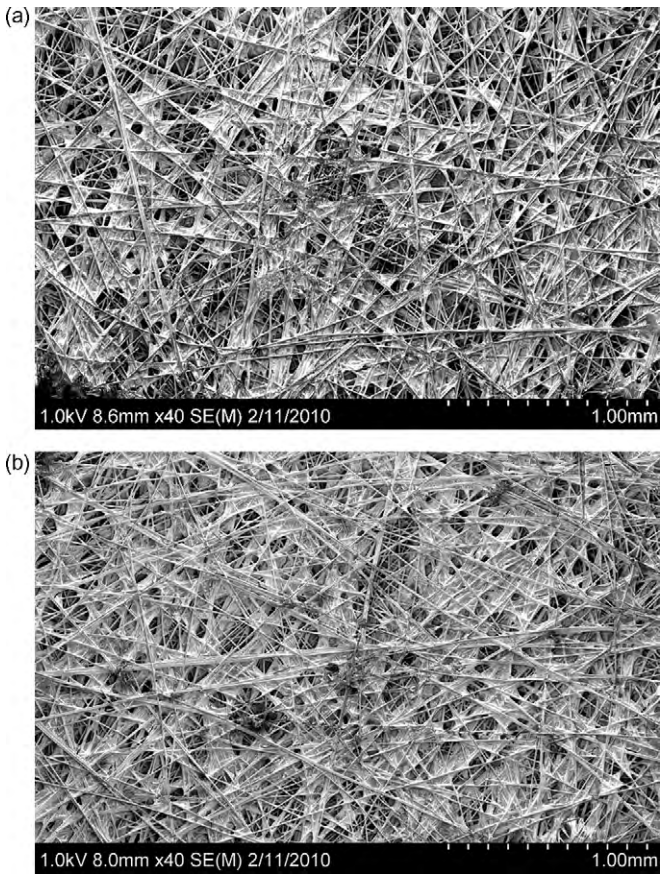

Fig. 2. SEM images of Toray carbon papers with 5% PTFE treatment and porosity of 78% before the experiments, ×40 magnification (a) TGP-H-120 with t_0 = 0.37 mm and (b) TGP-H-060 with t_0 = 0.19 mm.

corresponding to the lower threshold for natural convection [22], it is reasonable to assume negligible natural convection inside the GDL sample for the ambient pressure tests.

Radiation heat transfer between the fibers is also negligible since the temperature difference between fibers is small and the absolute temperature levels in the samples during the tests remain relatively low, i.e. less than 100 °C (373 K). Thus, the heat transfer through the fluxmeters is only due to diffusion through the fibers and air (atmospheric tests) and can be determined using Fourier's equation.

$$Q = -kA\frac{dT}{dz} \tag{1}$$

where dT/dz is the temperature gradient along the test column, k is the thermal conductivity of the fluxmeters, and A is the cross-sectional area of samples/fluxmeters. The temperatures at the top and bottom contact surfaces can be extrapolated through the measured heat flux. The total thermal resistance of the sample, R_{tot}, includes the sample thermal resistance and the thermal contact resistance (at the top and bottom surfaces) and can be expressed as:

$$R_{tot} = R_{GDL} + TCR = \frac{\Delta T_{ul}}{Q} \tag{2}$$

where ΔT_{ul} is the temperature difference between the upper and the lower contact surfaces. R_{GDL} and TCR are the GDL resistance and the total contact resistance, respectively. There are two interfaces between the GDL and the fluxmeters; it is assumed that the contact resistance at the top and bottom of the GDLs are equal; $TCR_{up} = TCR_{low} = (TCR/2)$.

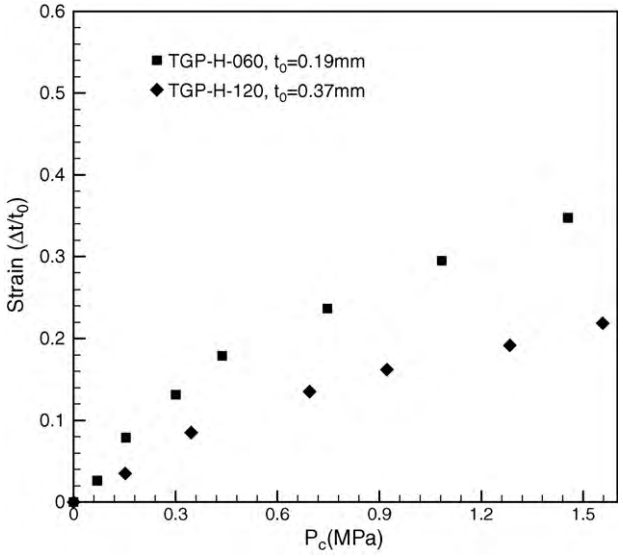

Fig. 3. Thickness variation of Toray carbon paper TGP-H-060 and TGP-H-120 under compression.

To deconvolute thermal conductivity and *TCR*, two experiments were performed with samples of different thicknesses; but with identical micro-structural parameters. Under the same pressure, the *TCR* for both samples is assumed to be equal. Applying Eq. (2) to both measurements and subtracting them yields the effective thermal conductivity:

$$k_{eff} = \frac{t_1}{R_{GDL1}A} = \frac{t_2}{R_{GDL2}A} \tag{3}$$

$$k_{eff} = \frac{t_1 - t_2}{(R_{tot1} - R_{tot2})A} \tag{4}$$

where t_1 and t_2 are the thicknesses of samples 1 and 2, respectively at the specific applied pressure, and A is the cross-section of samples. Eq. (4) can be used to find the effective thermal conductivity; the *TCR* can then be calculated by Eq. (2).

2.2. Mechanical test

The thickness variation of Toray carbon papers TGP-H-060 and TGP-H-120 under different compressive loads was measured using a tensile-compression apparatus. A Mitutoyo digital indicator with a 0.001 mm resolution was used to measure the thickness variation under compression. The GDL samples were cut in a circular shape of 25 mm diameter and then compressed by a steel rod using a pneumatic actuator. Various compression forces were applied on the GDL using the apparatus. A load cell with an accuracy of 2.5% was placed on the top of the samples. The load was increased at 15–20 min intervals to ensure mechanical equilibrium and steady-state condition. Measurements were repeated five times for each sample and the averaged values are reported in this work (see Fig. 3).

2.3. Uncertainty analysis

Considering the relationships for evaluating the effective thermal conductivity and the thermal contact resistance, i.e. Eqs. (4) and (2), the relevant parameters in the analysis can be expressed as:

$$R_{tot} = f(Q, \Delta T, t, A, P_c) \tag{5}$$

The main uncertainty in these experiments is due to errors in determining the heat flux through the sample which leads to

Table 1
Uncertainty of involving parameters in the analysis.

$\delta Q/Q$	$\delta \Delta T/\Delta T$	$\delta t/t$	$\delta A/A$	$\delta P_c/P_c$
4.3%	1.3%	2.7%	1.6%	2.5%

a maximum error of 4.3%. The maximum uncertainties for the thermocouples and the data acquisition readings are ±1 °C which introduces a maximum error of 1.3% between the interfaces of the sample and fluxmeters. Other uncertainties including those associated with the load cell, thickness, and cross-sectional area measurements and are listed in Table 1. The maximum uncertainty for the thermal resistance measurements can be calculated from [23]:

$$\frac{\delta R_{tot}}{R_{tot}} = \sqrt{\left(\frac{\delta Q}{Q}\right)^2 + \left(\frac{\delta \Delta T}{\Delta T}\right)^2 + \left(\frac{\delta t}{t}\right)^2 + \left(\frac{\delta A}{A}\right)^2 + \left(\frac{\delta P_c}{P_c}\right)^2} \quad (6)$$

For the present study, the maximum uncertainty is estimated to be ±6%.

3. Analytical study

3.1. Thermal conductivity model

To determine the through-plane effective thermal conductivity of fibrous GDL, a unit cell approach is employed [11]. The goal of this approach is to model the random and anisotropic structure of GDL with a relatively simple geometry which can predict the effective thermal conductivity accurately. The proposed geometrical model is shown in Fig. 4 and consists of uniformly sized equally spaced cylindrical fibers immersed in stagnant air. The fibers angle, θ, can be varied in this model.

Although the fibers are randomly oriented in practice, the averaged effect of this randomness on the transport properties of a sample is well represented by n unit cells with an orthogonal arrangement as shown in Sadeghi et al. [11] comparison of model predictions and experiments; this is corroborated by the recent results of Van Doormaal and Pharoah [24]. Thus, in the present study, the orthogonal and square arrangement of fibers is considered. The micro-structure of carbon papers is deformed non-linearly with the compressive load as shown in Fig. 3. This non-linear deformation is a complex combination of elastic and plastic deformations and slippage and breakage of fibers, binders, and PTFE which is clear in Fig. 5. We modeled this deformation as a combination of elastic deformation and slipping of fibers. A schematic of the deformation of the unit cell under the load is shown in Fig. 6. The total thickness reduction is the summation of elastic deformation and thickness variation as a result of fiber slippage.

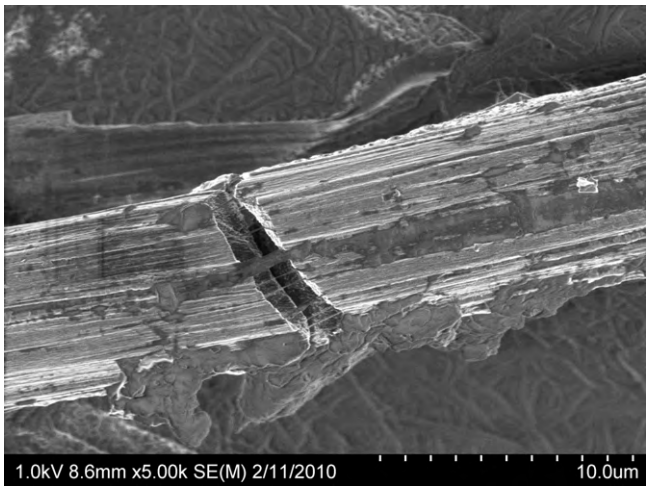

Fig. 5. SEM image of a broken TGP-H-120 fiber after compression, ×5000 magnification.

$$\delta_{tot} = \delta_s + \delta_e = \epsilon \cdot d \quad (7)$$

where d is the mean diameter of fibers and δ_e and δ_s are the thickness reductions as a result of elastic deformation and fiber slippage, respectively. The deformation of the carbon paper under the load shown in Fig. 3 is correlated by

$$\varepsilon = \frac{\Delta t}{t_0} = \begin{cases} 0.274[1 - \exp(-0.988P_c^*)] : \text{TGP-H-120} \\ 0.449[1 - \exp(-1.063P_c^*)] : \text{TGP-H-060} \end{cases} \quad (8)$$

where P_c^* is the contact pressure in MPa non-dimensionalized with respect to the reference pressure P_0 = 1 MPa.

To find the contact area between fibers, the Hertzian contact theory [7] is applied. Based on this theory, when a cylindrical fiber

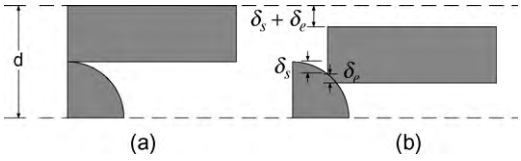

Fig. 6. Contacting fibers in the unit cell: (a) before compression and (b) after compression.

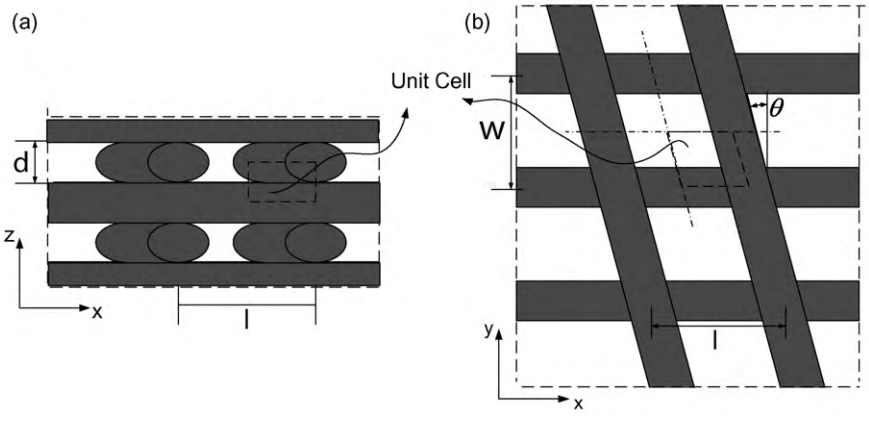

Fig. 4. Geometrical model of GDL: (a) front view and (b) top view [10].

contacts another cylindrical fiber eccentrically, as is the case here, the contact spot is close to an ellipse and the relation between the elastic deformation δ_e and the load F can be expressed approximately in the terms of deformations as [7]:

$$F = \frac{4}{3}E^* R_e^{1/2}\delta_e^{3/2} \tag{9}$$

where R_e is the equivalent radius of the principal radii of curvature of two contacting bodies which is equal to the average fiber radius for the present study. E^* is the effective Young's modulus which can be defined as a function of Young's modulus and Poisson's ratio of two contacting bodies [7].

$$E^* = \left(\frac{1-\nu_1{}^2}{E_1} + \frac{1-\nu_2{}^2}{E_2}\right)^{-1} \tag{10}$$

The major and minor radii of the contact area can be found from the geometrical relations of the deformed unit cell shown in Fig. 6(b).

$$a = \sqrt{r^2 - (r-\delta_e)^2} \tag{11}$$

$$b = \sqrt{r^2 - (r-\delta_e-\lambda)^2} - \sqrt{r^2-(r-\lambda)^2} \tag{12}$$

where λ is the onset of elastic deformation, the thickness variation before the start of the elastic deformation. Through a comparison with experimental data, λ is found to be $\delta_s/60$ and $\delta_s/15$ for TGP-H-060 and TGP-H-120, respectively. Comparison of different thermal resistances against the heat transfer in the unit cell indicates that the constriction/spreading resistance R_{sp} is the controlling resistance [11]. Thus to develop a compact model, the contributions of other resistances can be neglected. When heat flows in/out of a body through a small area, the heat flux lines are correspondingly constricted/spread apart and the resulting thermal resistance is referred to as constriction/spreading resistance. The spreading resistance can be approximated by the solution of an elliptical heat source on a circular flux tube given by [25]:

$$R_{sp} = \frac{1.6974}{\pi^2 k_s b}\psi(\alpha)\cdot\kappa\left(1-\frac{a^2}{b^2}\right) \tag{13}$$

where $\psi(\alpha)$ is the constriction parameter which can be expressed as [26]:

$$\psi(\alpha) = (1-\alpha)^{1.5} \tag{14}$$

where α is the ratio of the contact size to the fiber radius, $\alpha = \sqrt{ab}/r$. $\kappa(\cdot)$ is the complete elliptic integral of the first kind defined as

$$\kappa\left(1-\frac{a^2}{b^2}\right) = \int_0^{\pi/2}\frac{dt}{\sqrt{1-(1-(a^2/b^2))\sin^2 t}} \tag{15}$$

The effective thermal conductivity of GDL can be found through the relationship between the total thermal resistance and the effective thermal conductivity:

$$k_{eff} = \frac{t_{uc}}{R_{tot}A_{uc}} = \frac{d(1-\varepsilon)}{2R_{sp}A_{uc}} \tag{16}$$

where t_{uc} is the thickness of the unit cell under compression and A_{uc} is the cross-sectional area of the unit cell with the width of $w/2$, $A_{uc} = w^2/4$.

3.2. Thermal contact resistance model

All surfaces are inherently rough and the actual contact area consists of microscopic scale interfaces between asperities of the two contacting bodies. Therefore, the topologies of both contacting surface are important in understanding their interfacial behavior

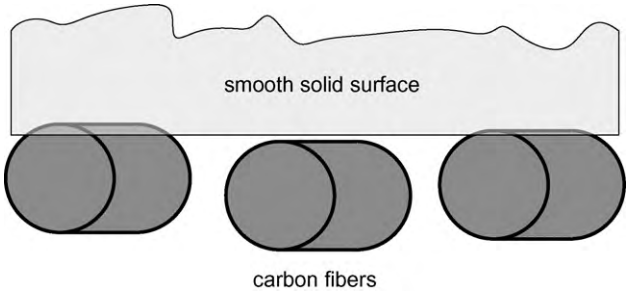

Fig. 7. GDL fibers in contact with a smooth solid surface.

[18]. To verify our experimental data for *TCR*, an analytical model is developed using the Greenwood and Williamson statistical model [27]. This model is based on the Hertz solution for individual elastic contacts and assumes that only asperities originally higher than the separation of the surfaces are in contact. Also, the model only considers the solid microcontacts corresponding to the vacuum condition.

The surface roughness of the fluxmeters and carbon papers are measured using a Mitutoyo profilometer. The average roughness for the fluxmeters is less than 1 μm which is insignificant compared to the average pore size and fiber diameter, and therefore these surfaces can hence be considered smooth. A schematic of the contact between a smooth solid surface and carbon fibers of GDL in Fig. 7 shows that only a small portion of the solid surface is in contact with the fibers.

For carbon papers with high porosity and a random fiber distribution on the surface, it is complicated to define roughness parameters. In this study, we assumed that the carbon paper surface acts as a rough solid surface and we determined the roughness parameters through profilometry. The measured parameters, averaged data for TGP-H-120 and TGP-H-060, are shown in Table 2. The asperity radius is assumed to be equal to the average fiber radius, $R_p = r = 4.25$ μm.

The total contact force can be found by [27]:

$$F = P_c A_0 = N\int_h^\infty \frac{4}{3}E^* R_e^{1/2}(z-h)^{3/2}\phi(z)dz \tag{17}$$

where N is the total number of contact points and h is the separation of the surfaces. P_c and A_0 are the contact pressure and the nominal contact area, respectively. $\phi(z)$ is the normal distribution of the surface height which can be described as

$$\phi(z) = \frac{1}{\sigma\sqrt{2\pi}}\exp\left(-\frac{z^2}{2\sigma^2}\right) \tag{18}$$

where σ is the root mean square of the surface roughness. Since the deformation of GDL under compression is significant, a portion of the force F is absorbed for the thickness reduction. To find the actual contact area, the thickness reduction of the unit cell close to the contact surface should be subtracted from the total deformation. The radius of a contact spot at the distance z from the separation line of the contacting surfaces can be expressed as [7]:

$$a(z) = \sqrt{(z-h-\epsilon\delta)R_p} \tag{19}$$

The contact resistance of this contact spot can be written as the summation of the constriction resistance in the fluxmeter and the

Table 2
Input data for *TCR* modeling of Toray carbon papers.

σ (μm)	D_{peak} (mm^{-1})	E_c (GPa)	$E_{\perp}$ (GPa)	K_c (W m^{-1} K^{-1})	k_{fl} (W m^{-1} K^{-1})
8.96	12.6	3.2	210	120	66

spreading resistance in the adjunct carbon fiber.

$$R(z) = \frac{1}{4k_{fl}a(z)} + \frac{1}{4k_c a(z)} \tag{20}$$

Therefore, the total contact resistance can be expressed as the parallel combination of all contact spots.

$$TCR = \left(\frac{2Nk_{fl}k_c \int_{h+\varepsilon d}^{\infty} \sqrt{(z-h-\varepsilon d)R_p}\phi(z)dz}{k_{fl}+k_c} \right)^{-1} \tag{21}$$

where k_{fl} and k_c are the thermal conductivities of the fluxmeters and the carbon fiber, respectively. For more convenience in evaluating integrals and performing parametric studies, a code was written in Fortran for the *TCR* and effective thermal conductivity modeling.

4. Results and discussion

The measurements were taken at different compressive loads in a vacuum as well as under ambient pressure condition to study the effects of the compressive load and the contribution of heat conduction in air on *TCR* and effective thermal conductivity.

Fig. 8(a) shows the temperature variation along the test column (upper and lower fluxmeters) for TGP-H-120 Toray carbon paper at atmospheric pressure. As expected, the temperature variation is linear along the column; the small difference in the upper and the lower fluxmeters slopes is a result of the temperature difference, since the fluxmeters thermal conductivity is a function of temperature. Perfect thermal insulation (adiabatic conditions) cannot be achieved in practice and small thermal losses occur to the test structure and the surroundings as shown by the relative difference in heat transfer rates for the upper and lower fluxmeters in Fig. 8(b) at various compressive loads. The maximum difference is 4.1% at low pressures, decreasing to 1.4% for higher contact pressures.

The effective thermal conductivity values at different contact pressures are compared with the analytical model, Eq. (16), in Fig. 9 for vacuum and atmospheric pressure conditions. The effective conductivity increases with an increase in the compressive load due to larger size and number of contacts between the fibers. The manufacturer's effective thermal conductivity of 1.7 W m^{-1} K^{-1} differs by 4.4% from our result at a relatively low pressure of 0.478 MPa. A small difference (less than 3%) can be observed between thermal conductivity values obtained under atmospheric and vacuum conditions, indicating that the air trapped in gaps/pockets of the medium provide an additional, but relatively ineffective path for heat conduction. Comparison of the model predictions and experimental data shows good agreement for both vacuum and atmospheric pressure conditions and over a wide range of compressive loads.

Fig. 10 shows the thermal contact resistance of both types of Toray carbon papers under different compressive loads. Again, the present analytical model for *TCR* under vacuum condition, Eq. (21), correlates very satisfactorily (within 15%) with the experimental data.

Since air fills the gaps between the contact surfaces and provides another path for heat conduction across the contact interface, the thermal contact resistance and consequently the total thermal resistance decrease. This reduction is less pronounced at higher contact pressures when the contact area increases providing preferential thermal paths. Under both ambient and vacuum conditions, *TCR* decreases with an increase in compressive load due to the increased contact area. It should also be noted that increasing compression beyond a certain level induces fiber breakage and irreversible deformations [28]; this results in hysteresis effects under cyclic loads. These hysteresis effects will be studied in-depth in Part 2 of this study.

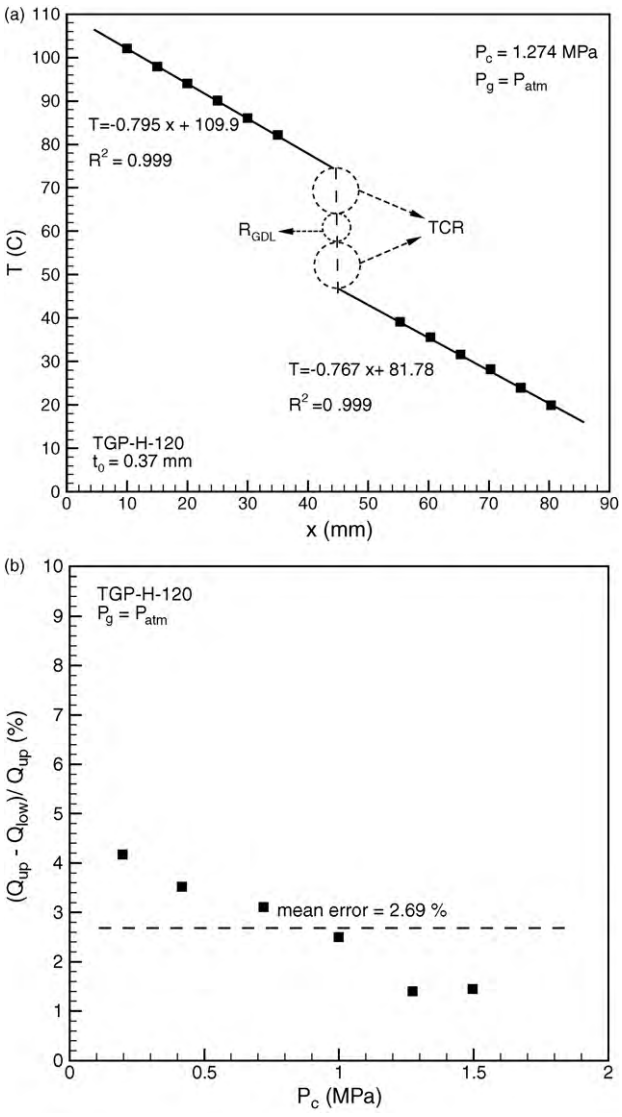

Fig. 8. (a) Temperature distribution along the test column; (b) relative difference in the heat flux passing through the upper and the lower fluxmeters.

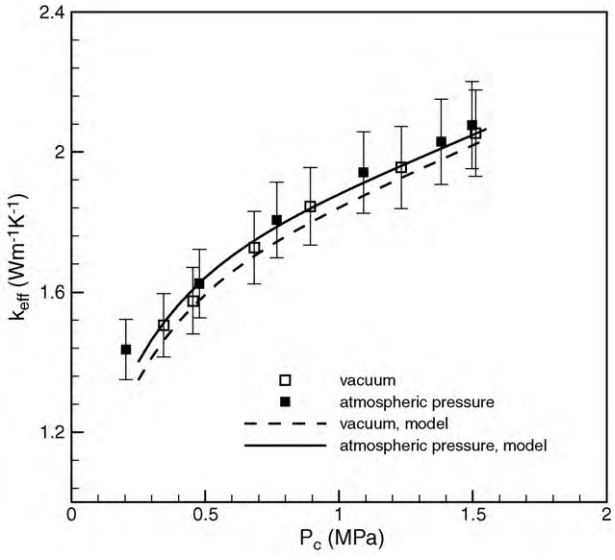

Fig. 9. Effective thermal conductivity of the Toray carbon papers at vacuum and atmospheric pressures: experimental data and model.

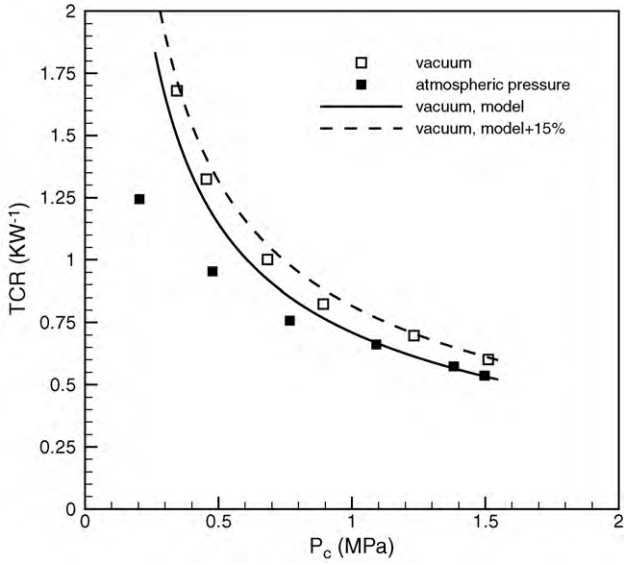

Fig. 10. Comparison of thermal contact resistance at vacuum and atmospheric pressure.

Fig. 11 shows the *TCR* to total resistance ratio as a function of compression, and we observe that:

- *TCR* is clearly the dominant resistance, contributing between 65 and 90% of the total resistance.
- As expected, the relative contribution of *TCR* is more important for thinner materials; the average *TCR* ratio for TGP-H-120 and TGP-H-060 at atmospheric pressure is 68% and 82%, respectively.

Both thermal conductivity and *TCR* decrease with increasing compression; however, as shown in Fig. 11, the *TCR* to total resistance ratio remains approximately constant.

The variations of the total thermal resistance and of the effective thermal conductivity with temperature are shown in Fig. 12 for TGP-H-120 sample subjected to a constant contact pressure of 0.75 MPa. The effective thermal conductivity decreases slightly with increasing temperature, while the total resistance remains approximately constant. Considering that the *TCR* is the controlling component of the total resistance, we can conclude that the

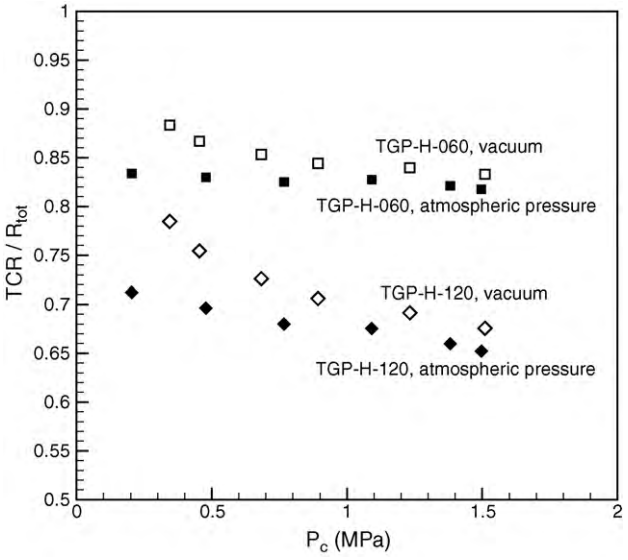

Fig. 11. Thermal contact resistance to total resistance ratio at different pressures.

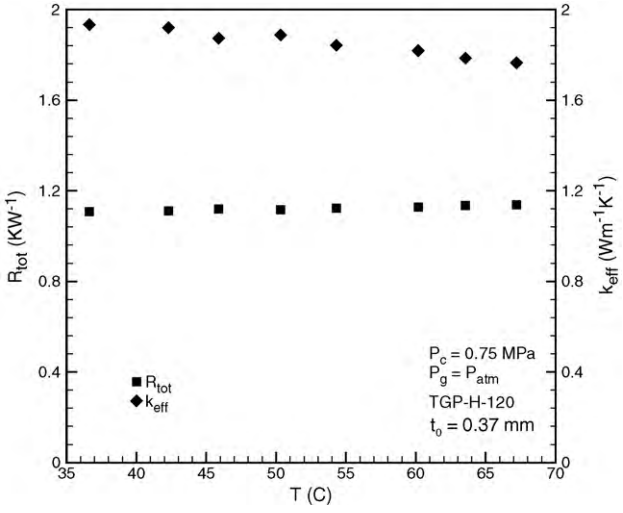

Fig. 12. Effect of operation temperature on the total thermal resistance.

TCR does not depend on temperature, at least in the range of temperatures considered here.

The reduction in thermal conductivity can be attributed to the presence of carbonized thermo-setting resins used as a binder in GDLs [29]. The thermal conductivity of these thermo-setting polymers decreases with increasing temperature [30], and this would result in a reduction in the effective thermal conductivity of the medium.

5. Summary and conclusions

A test bed was designed and built and analytic models were developed to measure and predict thermal conductivity and thermal contact resistance of GDLs under various compressive loads. The model predictions are in good agreement with experimental data over a wide range of compressive loads from 0.2 to 1.5 MPa. Parametric studies performed to investigate the trends and effects of compression, conduction in air, and operating temperature show that the effective thermal conductivity increases with the compressive load and decreases with an increase with operating temperature, but that it is relatively insensitive to ambient air pressure. An important finding is the dominant contribution of thermal contact resistance to the total thermal resistance. The ratio of thermal contact to bulk GDL resistance remains approximately constant, e.g. (4.6/1) for TGP-H-060 at atmospheric pressure over a range of conditions.

This work has helped clarify the impact of several operational parameters on the thermal properties of GDLs and provided new insights on the importance of a key interfacial phenomenon. Further work will be required to investigate the effect of cycling changes in conditions encountered in operating fuel cell stacks, and to extend the measurements and theoretical analysis to other MEA interfaces, such as that between the micro-porous layer and the GDL.

Acknowledgements

The authors are grateful for the financial support of the Natural Sciences and Engineering Research Council (NSERC) of Canada, and the Canada Research Chairs Program.

References

[1] N. Djilali, D. Lu, Int. J. Therm. Sci. 41 (2002) 29–40.
[2] T. Berning, N. Djilali, J. Electrochem. Soc. 150 (2003) A1589–A1598.

[3] S. He, M.M. Mench, S. Tadigadapa, Sens. Actuators A: Phys. 125 (2006) 170–177.
[4] P.J.S. Vie, S. Kjelstrup, Electrochim. Acta 49 (2004) 1069–1077.
[5] A. Kusoglu, Y. Tang, M.H. Santare, A.M. Karlsson, S. Cleghorn, W.B. Johnson, J. Fuel Cell Sci. Technol. 6 (2009) 011012–011019.
[6] A. Kusoglu, A.M. Karlsson, M.H. Santare, S. Cleghorn, W.B. Johnson, J. Power Sources 161 (2006) 987–996.
[7] K.L. Johnson, Contact Mechanics, Cambridge Univ. Press, London, UK, 1985, Ch. 4, 13.
[8] J. Ramousse, S. Didierjean, P. Lottin, D. Maillet, Int. J. Therm. Sci. 47 (2008) 1–6.
[9] A. Hakenjos, H. Muenter, U. Wittstadt, C. Hebling, J. Power Sources 131 (2004) 213–216.
[10] F. Danes, J.P. Bardon, Revue Générale de Thermique 36 (1997) 302–311.
[11] E. Sadeghi, M. Bahrami, N. Djilali, J. Power Sources 179 (2008) 200–208.
[12] J. Becker, V. Schulz, A. Wiegmann, J. Fuel Cell Sci. Technol. 5 (2008) 21006–21015.
[13] M. Wang, J. He, J. Yu, N. Pan, Int. J. Therm. Sci. 46 (2007) 848–855.
[14] M. Khandelwal, M.M. Mench, J. Power Sources 161 (2006) 1106–1115.
[15] I. Nitta, O. Himanen, M. Mikkola, Fuel Cells 08 (2008) 111–119.
[16] O. Burheim, P.J.S. Vi, J.G. Pharoah, S. Kjelstrup, J. Power Sources 195 (2010) 249–256.
[17] V. Mishra, F. Yang, R. Pitchumani, J. Fuel Cell Sci. Technol. 1 (2004) 2–9.
[18] Y. Zhou, G. Lin, A.J. Shih, S.J. Hu, J. Power Sources 163 (2007) 777–783.
[19] Z. Wu, S. Wang, L. Zhang, S.J. Hu, J. Power Sources 189 (2009) 1066–1073.
[20] T. Swamy, E.C. Kumbar, M.M. Mench, J. Electrochem. Soc. 157 (2010) B77–B85.
[21] S. Escribano, J.-F. Blachot, J. Etheve, A. Morin, R. Mosdale, J. Power Sources 156 (2006) 8–13.
[22] V.S. Arpaci, P.S. Larsen, Convection Heat Transfer, Prentice-Hall, Englewood Cliffs, NJ, 1984, Ch. 4.
[23] J.R. Taylor, An Introduction to Error Analysis: The Study of Uncertainties in Physical Measurements, second ed., University Science Books, Sausalito, US, 1997, Ch. 3.
[24] M.A. Van Doormaal, J.G. Pharoah, Int. J. Numer. Meth. Fluids 59 (2009) 75–89.
[25] M.M. Yovanovich, Progr. Astronaut. Aeronaut.: Radiat. Trans. Therm. Control 49 (1976) 397–418.
[26] M.G. Cooper, B.B. Mikic, M.M. Yovanovich, Int. J. Heat Mass Trans. 12 (1969) 279–300.
[27] J.A. Greenwood, B.P. Williamson, Proc. R. Soc. London: Ser. A: Math. Phys. Sci. 295 (1966) 300–319.
[28] A. Bazylak, D. Sinton, Z.-S. Liu, N. Djilali, J. Power Sources 163 (2007) 784–792.
[29] M.F. Mathias, J. Roth, J. Fleming, W. Lehnert, in: W. Vielstich, H.A. Gasteiger, A. Lamm (Eds.), Handbook of Fuel Cells-Fundamental, Technology and Application, vol. 3, John Wiley & Sons, Ltd., 2003, pp. 517–537.
Books, Sausalito, US, 1997, Ch. 3.
[24] M.A. Van Doormaal, J.G. Pharoah, Int. J. Numer. Meth. Fluids 59 (2009) 75–89.
[25] M.M. Yovanovich, Progr. Astronaut. Aeronaut.: Radiat. Trans. Therm. Control 49 (1976) 397–418.
[26] M.G. Cooper, B.B. Mikic, M.M. Yovanovich, Int. J. Heat Mass Trans. 12 (1969) 279–300.
[27] J.A. Greenwood, B.P. Williamson, Proc. R. Soc. London: Ser. A: Math. Phys. Sci. 295 (1966) 300–319.
[28] A. Bazylak, D. Sinton, Z.-S. Liu, N. Djilali, J. Power Sources 163 (2007) 784–792.
[29] M.F. Mathias, J. Roth, J. Fleming, W. Lehnert, in: W. Vielstich, H.A. Gasteiger, A. Lamm (Eds.), Handbook of Fuel Cells-Fundamental, Technology and Application, vol. 3, John Wiley & Sons, Ltd., 2003, pp. 517–537.
[30] C.L. Choy, Y.W. Wong, G.W. Yang, T. Kanamoto, J. Polym. Sci.: Polym. Phys. 37 (1999) 3359–3367.